# Heat transfer and energy storage performances of phase change materials encapsulated in honeycomb cells

Karunesh Kant, Pascal Henry Biwole, A. Shukla, Atul Sharma, Shiva Gorjian

Version of Record: https://www.sciencedirect.com/science/article/pii/S2352152X21002565
Manuscript_c4724ee145eece04a67c412f9053f26e

# Heat Transfer and Energy Storage Performances of Phase Change Materials Encapsulated in Honeycomb Cells

K. Kant[a,1], P. H. Biwole[a,d], A. Shukla[b], Atul Sharma[b], Shiva Gorjian[c]

[a] Université Clermont Auvergne, CNRS, Clermont Auvergne INP, Institut Pascal, F-63000 Clermont–Ferrand, France

[b] Non-Conventional Energy Laboratory, Rajiv Gandhi Institute of Petroleum Technology, Jais, Amethi, UP, India

[c] Biosystems Engineering Department, Faculty of Agriculture, Tarbiat Modares University (T.M.U.), Tehran, Iran

[d] MINES Paris Tech, PSL Research University, PERSEE - Center for Processes, Renewable Energies and Energy Systems, CS 10207, 06 904 Sophia Antipolis, France

[1] Corresponding author: k1091kant@gmail.com

## Abstract

Thermal energy storage devices are vital for reducing the inconsistency between energy supply and demand as well as for enhancing the performance of solar thermal systems. The present study investigates the melting process in metallic honeycombed heat exchangers filled with n-octadacane as phase change material (PCM). Further, a parametric study is conducted for four different honeycomb cell sizes, fin thicknesses, and angles of inclinations of the computational domain. The findings are described in the form of heated surface average temperature variation, melt fraction of the PCM, and thermal energy stored. Results show that the honeycomb fin structure considerably improves the heat transfer in the PCM. Further, it was observed that the honeycomb cell size and fin thickness greatly influence the variation of the average front surface temperature, melt fraction, and energy storage rate, whereas the inclination angle doesn't have a significant effect when cell size is less than 0.01 m. From the study, it was also observed that when the computational domain is horizontal without honeycomb cells, the pure conduction in the PCM results in much higher front surface temperature, which is greatly reduced in presence of the honeycomb cells.



Keywords: Phase change materials; Thermal energy storage; Numerical simulation; Heat transfer; Melt fraction

Nomenclature

| | |
|---|---|
| $C_p$ | specific heat [J/(kgK)] |
| $h_\infty$ | heat transfer coefficient on the front and back surface [W/(m$^2$K)] |
| $H$ | height of computational domain [m] |
| $k$ | thermal conductivity [W/(mK)] |
| $L_c$ | cell length [m] |
| $L_f$ | latent heat of PCM [J/kg] |
| $P$ | pressure [Pa] |
| $Pe$ | peclet number [1] |
| $q_0$ | incident heat flux on the front surface [W/m$^2$] |
| $t$ | time [s] |
| $T$ | temperature [K] |
| $T_\infty$ | ambient temperature [K] |
| $T_{ini}$ | initial temperature [K] |
| $u$ | velocity field of melted PCM[m/s] |
| $W$ | width of the computational domain [m] |
| $\delta_{fin}$ | fin thickness [m] |
| $\theta$ | tilt angle from horizontal [$^o$ ] |
| $\rho$ | density [kg/m$^3$] |
| $\rho_l$ | density of liquid PCM [kg/m$^3$] |
| $\rho_l$ | density of solid PCM [kg/m$^3$] |
| $\beta$ | thermal expansion coefficient of PCM [1/K] |
| $\mu$ | viscosity of melted PCM [Pa.s] |

Subscript

| | |
|---|---|
| $s$ | solid |
| $l$ | liquid |

# 1. INTRODUCTION

Solar energy is an abundantly available, clean, and sustainable energy source therefore it is accepted as one of the most favorable alternative energy sources for sustainable development [1–5]. Due to the intermittency by its nature, unreliability is the major impeding factor for the massive use of solar energy in agriculture and food processing. The unreliability of solar energy utilization can be diminished by stowing solar energy when it is excess compared to the demand and consuming the stowed energy whenever required. The energy storage system is, consequently, important to any system that is based largely on solar energy. Solar energy can be stored in the form of thermal energy in thermal energy storage (TES) devices. During the past few decades, the latent heat TES devices using PCM have gained larger attention due to their favorable thermophysical properties. However, these materials show poor thermal conductivity, which restricts the thermal transport in the storage medium and alleviates the melting/solidification process. To evade this shortcoming and enhance thermal transport throughout the solid-liquid phase transition, multitudinous approaches have been recommended in past studies. These approaches are the addition of highly thermal conductive nanoparticles [6–8], incorporation of metal matrix [9], addition porous matrices [10], and use of multiple PCMs [11,12]. Amid these approaches, the incorporation of the metal matrix in PCM is the focus of the present study because it is cheap and easy to integrate with the system.

In recent years, several studies have been executed to assess the heat transfer behavior of metal matrices integrated PCMs. In this regard, Biwole et al. [13] conducted a numerical simulation of RT-25 PCM filled in a rectangular enclosure to assess the effect of fin size and distribution. The effective fin configuration was investigated and it was perceived that the fin surface area is an important factor that guides the melting of PCM and the rate of heat transfer between the PCM and the front hot surface, while the fin structures advance greater natural convection, leading to an advanced heat flux. Groulx et al. [14] conducted a numerical simulation to assess the influence of fin placement and angle of inclination on the melting of RT25 PCM in a rectangular enclosure. Based on the study it was concluded that the convection heat transfer causes a significant acceleration in the melting process of the PCM. Also, a negligible effect for the computational domain's inclination angle smaller than 75° from vertical on the heat transfer behavior of all considered configurations was reported. Darzi et al. [15] studied the melting and solidification behavior of PCM considering radial

fins and thermally conductive nanoparticles to enhanced thermal transport. The phase change process was accelerated by increasing the nanoparticle concentration and the elliptical tube decreases the melting time as compared to the circular tube. Further, increment the fin number show system deficient due to the suppression of natural convection. A numerical study of PCM solidification was conducted by Abidi et al [16] to investigate the best configuration that minimizes the melting and solidification time of PCM in a triplex tube heat exchanger with both external and internal fins. In continuation with the thermal transport enhancement using fin structure, a novel snowflake crystal fin structure was investigated by Sheikholeslami et al. [17] to enhance the thermal efficiency of the latent heat thermal energy storage (LHTES) device during the heat discharging process. The obtained results were indicated that the discharging process of the LHTES is improved by applying Snowflake shaped fin structure, in comparison with the nanoparticle diffusion, while it does not considerably reduce the maximum thermal energy storage capacity. Wu et al. [18] performed numerical analysis and improved the thermal transport behavior of the LHTES device with spiderweb-like fins. From the obtained results it is observed that the spiderweb-like fins decrease melting and solidification time by reducing the heat transfer hysteresis region.

In the recent past, several investigators have made substantial efforts to improve the thermal performance of LHTES devices by using different thermally conductive fin structures. The researchers had paid their most attention toward modified rectangular and annular fin structures. Conversely, several studies have shown that proposed conventional fins have a simple structure with a small specific surface area which makes it tough to realize reasonable thermal transport performance of LHTES devices. Consequently, some fins with mixed structures and a high specific surface have been found to enhance the thermal transport effectiveness of LHTES devices. Recently, bionics are advanced in the field of fluid flow and heat transfer applications including chemical reactor [19], biomedical equipment [20,21], and electronic cooling [22–26]. The fin structures made by natural assortment encourages the improvement of the LHTES device. By realizing natural structures, the fins with bionic structures for instance tree-shaped fins [26,27], Koch fractal fins [28], and snowflake-shaped fins [17,29] have been recently proposed by researchers to the enhanced thermal performance of PCM thermal energy storage devices.

The bionic fins provide an effective means for thermal transport, therefore increasing the thermal transport effectiveness of LHTES devices. Though the hysteresis exists during

melting and solidification of PCM with various ranges depends on the gaps between fins. The presence of hysteresis impedes the additional enhancement of the thermal efficiency of such devices. The extensive existence of honeycomb meshed structure in nature offers an idea to solve the hysteresis problem. As shown in *Figure 1*, the honeycomb has a compact and uniformly distributed structure over the entire structure. Based on this quality, the use of honeycomb-like fin introduces a high interest for improved efficiency of charging and discharging processes of LHTES devices.

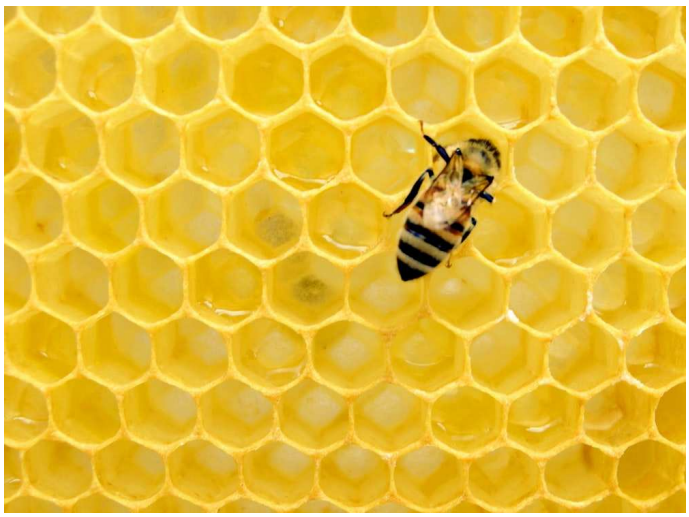

*Figure 1 Honey bee honeycomb*

Through a comprehensive literature assessment, it can be chronicled that not much investigation has been dedicated to investigating the charging efficiency of LHTES devices with honeycomb meshed fins. The melting behavior of PCM and interstitial thermal energy absorption process between honeycomb meshed fin structures and PCM is still imprecise. Further, the effect of the honeycomb meshed fin structure on the charging efficiency of LHTES devices has not been exposed so far. The effect of natural convection on the melting progression has been highlighted by numerous researchers; however, no known study has been found in the literature on the melting and energy storage behavior of PCM in the honeycomb structure and limited works have focused on the effect of the container's tilt angle on the melting behavior of the PCM process. Consequently, the current analysis provides an advanced insight into how the thorough nature of honeycomb meshed fins influence the heat absorption behavior of LHTES devices while can be considered as an important work to enhance the thermal storage and discharge effectiveness.

The article is structured as follows: In the introduction section, the overall background and the goal of the current study are presented. After the introduction, the computational model with all the simulation details including the dimensions and constants used in the study are described. Next to the computational model, the mathematical formulation, boundary conditions, and computational technique with model validation are presented. Further, detailed discussions on the results of the present study are presented, trailed by a summary of the key conclusions.

## 2. COMPUTATIONAL MODEL

The geometry of the computational domain considered in the present work has been presented in Figure 2. The computational domain is poised of two vertical metallic plates connected with hexagonal honeycomb cells; the fin thickness of each hexagonal cell, as well as the vertical plate, is $\delta_{fin}$. The height ($H$) and width ($W$) of the container are fixed, with values 0.077942 m and 0.045 m respectively and the inclination angle of the computational domain from horizontal is $\theta$ ° as shown in Figure 2. Each cell in the container has the same length ($L_C$) and uniform thickness. Internal fins are also made of the same material as front and back vertical plates. The cell length $L_C$, the inclination angle of the container from horizontal $\theta$ and the fin thickness are given in Table 2. The thermo-physical properties of metallic fins and PCM considered in the present study are shown in Table 1. The computational domain is primarily set at a temperature $T_{ini} = 23.2$ °C and the front metallic plate is subjected to a continuous heat flux of $q_0 = 1000\, W/m^2$ perpendicular to the front surface for the period of the numerical simulation. As the present study is only focused on the influence of honeycomb structure on the heat transfer behavior in PCM, the convective heat transfer coefficient on the front and back surface is fixed. The front and back surface of the container is opened to convection cooling with an ambient temperature of $T_\infty = 23.2$ °C as well as the convection heat transfer coefficient $h_\infty = 2\ W/m^2K$. The top and bottom of the computational domain are subjected to symmetry boundaries (adiabatic). The acceleration due to gravity is always working in the downward direction for the entire tilt angle range. To conduct numerical simulation the following assumptions has been considered in the present study: (i) the liquated PCM is incompressible and Newtonian, (ii) the melted PCM's flow is laminar, radiation and three-dimensional convection are neglected, (iii) volume expansion due to the melting of PCM is neglected.

In the present study, n-octadecane is considered as PCM and its thermo-physical properties are given in Table 1. Four different angles of inclination and fin thicknesses are studied for four different honeycomb cell sizes. The study has also been conducted without honeycomb cells in the rectangular plane of the container considered. The studied combinations of the fin thickness and inclinational angles are given in Table 2, where $L_C$ is the honeycomb cell length, $\delta_{fin}$ is the fin thickness of the honeycomb cells and $\theta$ is the angle of inclination of the computational domain from horizontal as shown in Figure 2. The numerical simulation was conducted at 4 different angles of inclination θ without honeycomb cells as well as at 4 different $L_C$ (i.e. $L_C$ = 0.005 m, $L_C$ = 0.0075 m, $L_C$ = 0.010 m and $L_C$ = 0.015 m) considering $\delta_{fin}$= 0.0005 m to investigate the effect of inclination angle as well as honeycomb cell length on front surface temperature, melt fraction, and energy storage content. Further, to investigate the effect of the honeycomb fin thickness, the studies are conducted at 4 different honeycomb fin thickness $\delta_{fin}$ with 4 honeycomb cell length $L_C$ while the angle of inclination of the computational domain is fixed at 60°. Through the change in honeycomb cell size, fin thickness, tilt angle from horizontal, initial, and boundary conditions to the mathematical model are described in the next section and thermal energy storage behavior of computational domain is described arrangements are described.

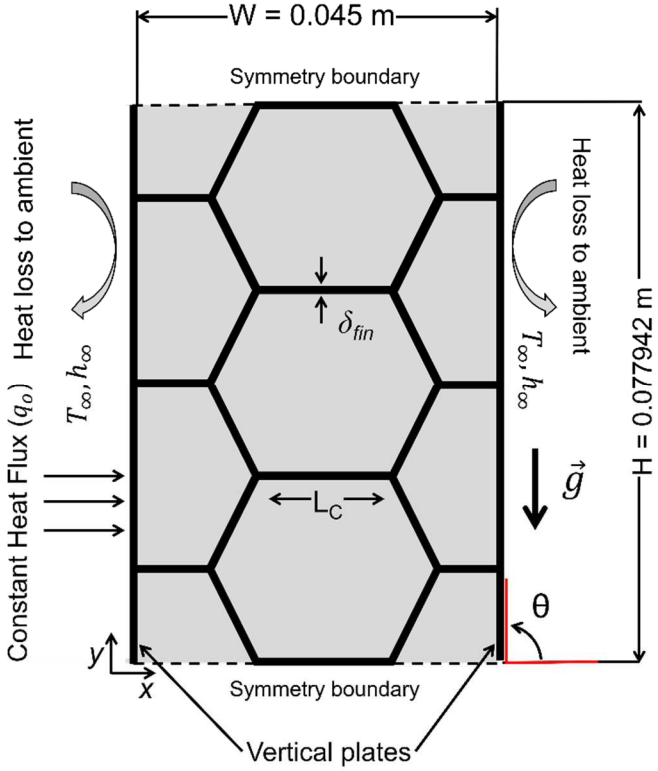


*Figure 2 Geometry and boundary conditions of the system considered for the numerical simulation*

*Table 1 Thermophysical properties of PCM and metallic fin*

| Properties /Material | PCM | Metallic fin |
|---|---|---|
| Melting temperature ($^oC$) | 28.2 | NA |
| Specific heat ($J/kg.K$) | 1934 ($s$), 2196 ($l$) | 900 |
| Latent heat of fusion ($kJ/kg$) | 245 | NA |
| Density ($kg/m^3$) | 814 ($s$), 775 ($l$) | 2700 |
| Thermal conductivity ($W/m.K$) | 0.350 ($s$), 0.149 ($l$) | 238 |
| Thermal expansion coefficient ($1/^oC$) | $9.1\times10^{-4}$ | NA |
| Kinematic viscosity ($m^2/s$) | $5\times10^{-6}$ | NA |

*Table 2 Parameters considered in the present study*

| | $\theta^o$ (at $\boldsymbol{\delta_{fin}}$= 0.0005 m) | | | | $\boldsymbol{\delta_{fin}}$ [m] (at $\theta$ = 60 $^o$) | | | |
|---|---|---|---|---|---|---|---|---|
| Without cells | 0 | 30 | 60 | 90 | NA | NA | NA | NA |
| $\boldsymbol{L_C = 0.005\ m}$ | 0 | 30 | 60 | 90 | 0.00025 | 0.0005 | 0.001 | 0.0015 |
| $\boldsymbol{L_C = 0.0075\ m}$ | 0 | 30 | 60 | 90 | 0.00025 | 0.0005 | 0.001 | 0.0015 |

| | | | | | | | | |
|---|---|---|---|---|---|---|---|---|
| $L_C = 0.010\ m$ | 0 | 30 | 60 | 90 | 0.00025 | 0.0005 | 0.001 | 0.0015 |
| $L_C = 0.015$ m | 0 | 30 | 60 | 90 | 0.00025 | 0.0005 | 0.001 | 0.0015 |

# 3. MATHEMATICAL FORMULATIONS

## *3.1. Numerical simulation model description*

The following equations (1) and (2) with the boundary conditions are applied on the heated front and back external surface correspondingly:

$$-k\frac{\partial T}{\partial x}\Big|_{x=0} = q_0 + h_\infty(T_\infty - T) \tag{1}$$

$$-k\frac{\partial T}{\partial x}\Big|_{x=\delta_{fin}+W+\delta_{fin}} = h_\infty(T - T_\infty) \tag{2}$$

Further, the equation of heat transfer diffusion realized within the fins and PCM domain is:

$$\rho C_p\frac{\partial T}{\partial t} + \nabla(-k\nabla T) + \rho C_p\vec{u}\cdot\nabla T = 0 \tag{3}$$

where $\rho$, $C_p$ and $k$ represents density, specific heat, and thermal conductivity respectively. For the PCM, the value of $\rho$, $k$ and $C_p$ varies with temperature as given by eq. (7), (8) and (9) respectively. The fluid velocity $\vec{u}$ is always zero in the metallic fins as well as on the surface of metallic fins, and is given in the PCM domain by numerically solving the Navier-Stokes and continuity equation; the equation of modified momentum conservation for the PCM domain can be given [14]:

$$\rho\frac{\partial\vec{u}}{\partial t} + \rho(\vec{u}\cdot\nabla)\vec{u} = -\nabla P + \rho_l\big(1-\beta(T-T_m)\big)\vec{g} + \mu_l\cdot\nabla^2\vec{u} - \frac{C(1-B(T))^2}{B^3(T)+\varepsilon}\,\vec{u} \tag{4}$$

where $\rho_l$ and $\mu_l$ are respectively the density and dynamic viscosity is of melted PCM, $\beta$ is the thermal expansion coefficient of PCM and $\vec{g}$ is the acceleration because of gravity constant. The value of constant C (Kozeny-Carman permeability) can be determined by the inherent characteristics of the PCM material. Increasing its value causes a decrease in the melted PCM's flow in the transition zone, and consequently to a smoother nature of the liquidus melting front while decreasing its value will have the contrary influence. The value of constant $C$ in the present study is $10^5$ kg/ ($m^3$·s). Here, ε is constant with a given value of

$10^{-3}$ as in [30] to evade dividing by zero. The melted fraction function $B(T)$ of PCM is defined as:

$$B(T) = \begin{cases} 0, & T < \left(T_m - \frac{\Delta T}{2}\right) \\ \frac{T - T_m + \Delta T/2}{\Delta T}, & \left(T_m - \frac{\Delta T}{2}\right) < T < \left(T_m + \frac{\Delta T}{2}\right) \\ 1, & T > \left(T_m + \frac{\Delta T}{2}\right) \end{cases} \quad (5)$$

Here $\Delta T$ is transition temperature and its value is taken 2°C in the present study. The varying thermo-physical properties of PCM are modeled as a function of temperature through Eqs. (6)-(10). The viscosity $\mu$ of PCM is adjusted to ensure a very high value when the PCM is in the solid-state [13].

$$\mu(T) = \mu_l \left(1 + \frac{C(1 - B(T))^2}{C_0(B^3(T) + \varepsilon)}\right) \quad (6)$$

$$\rho(T) = \rho_s + (\rho_l - \rho_s) \cdot B(T) \quad (7)$$

$$k(T) = k_s + (k_l - k_s) \cdot B(T) \quad (8)$$

where the value of $C_0$ is taken 1 kg/(m$^3$.s) to make sure unit consistency, $\rho_s$ and $\rho_l$ are the density of the solid and liquid phases of PCM, respectively. Similarly, the $k_s$ and $k_l$ are the PCM's thermal conductivity for solid and liquid phases respectively. The specific heat of PCM which is temperature-dependent modeled including an extra term which accounts for the latent heat of fusion stored or released in the melting or solidification process, consequential in an adjusted heat capacity of PCM can be given by [13]:

$$C_p(T) = C_{p_s} + \left(C_{p_l} - C_{p_s}\right) \cdot B(T) + L_f D(T) \quad (9)$$

where

$$D(T) = \frac{e^{\frac{-(T - T_m)^2}{(\Delta T/4)^2}}}{\sqrt{\pi(\Delta T/4)^2}} \quad (10)$$

The reason for considering the Gaussian function *D(T)* in eq. (9) is conserve the latent heat of PCM all over the transition period, because the integral of function *D(T)* over the whole range of transition temperature $\Delta T$ is always *1* [31]. The consideration of $\Delta T$ produces a

numerical mushy region. The mushy region thickness grows with the growth in the value of $\Delta T$. The value of $\Delta T$ depends on the nature of the materials and can be fixed empirically if one has previous information on the melting behavior of PCM. The deformation of geometry owing to the PCM's thermal expansion is not considered in the present study.

### *3.2. Computational method, meshing and validation of the model*

The above-mentioned equations are implemented in a fluid and laminar flow module of COMSOL Multiphysics 5.5. The present study used fixed-grid approaches similar to the one labeled in this section that consents to evade the necessity to solve the Stefan problem at the varying melting front. Furthermore, the melting front tracing method necessitates an already existed liquid layer, which is not the situation for the present study. Through fixed-grid approaches, the standard method for the liquid flow and energy for instance the finite element numerical resolution of N-S equations can be applied with partial modifications.

To solve the problem, an extremely fine mesh is chosen with a maximum and minimum size of the element of value $5.98 \times 10^{-4}$ m and $6.9 \times 10^{-6}$ m respectively, which results in the total number of 62716, 72050, 80806, and 95166 linear free triangular mesh elements for $L_C$ = 0.015 m, $L_C$ = 0.01 m, $L_C$ = 0.0075 m and $L_C$ = 0.0075 m respectively. The maximum mesh size is defined using a condition on the mass mesh Peclet number [31]:

$$Pe = \frac{\vec{u}\Delta x}{\vartheta} < 2 \tag{11}$$

where $\Delta x$ is the maximum length of mesh cell in a unit 2D surface. From numerical simulations, the maximum velocity in the honeycomb cell is taken as $5 \times 10^{-3}$ m/s. Therefore, Eq. (11) gives $\Delta x \approx 2 \times 10^{-3}$ m. In the present study, $Pe$ is kept lower than 1 to increase numerical stability. Consequently, the maximum mesh size is $1 \times 10^{-3}$ m. The mesh is refined at the borders of the PCM domain (see Figure 3). The first layer thickness of the boundary layer is $5.22 \times 10^{-5}$ m. Mesh sensitivity tests were also conducted at three increasing mesh element sizes and the transient average temperature of the container's front surface was observed at 38202, 50836, and 62716 mesh elements, as presented in Figure 4 for $L_C$ = 0.015 m. For the other $L_C$, the maximum and minimum mesh sizes are the same, therefore the change in the mesh size will not affect the output results from the model. From this figure, it is observed that there is a negligible change in the variation of the front surface temperature

when increasing the number of mesh elements. Therefore, for the sake of accuracy, maximum numbers of mesh elements were selected for the present study.

The numerical model presented above has been experimentally validated with our previous experimental study by Biwole *et al*. [31] and a comparison of the temperature variation is presented in *Figure 5*. For more details about the experimental setup and PCM properties, etc. please refer to Biwole *et al*. [31]. The model explained above has also been validated with the experimental results reported by Shokouhmand and Kamkari [32] on the Lauric acid's melting in another previous study conducted by Biwole et al. [13]. The verification of the model with previous experimental results provides the confidence for the detailed systematic parametric studies of honeycomb geometry for enhanced thermal transport in PCM.

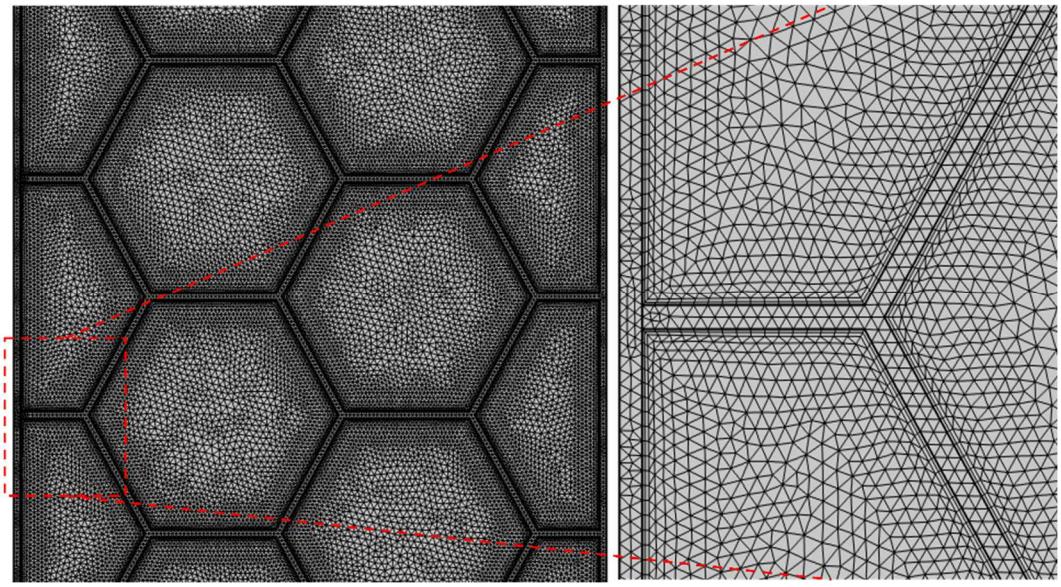

Reviewer 2,

*Figure 3 Meshing of the computational domain*

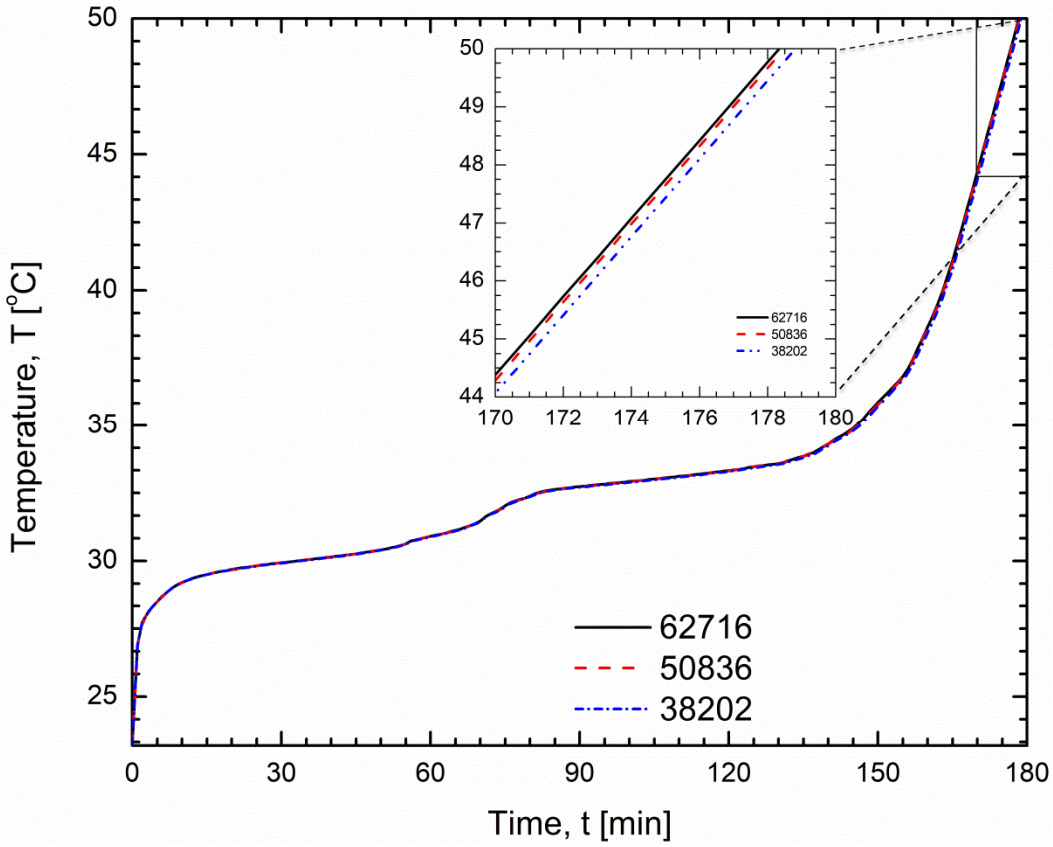


*Figure 4 Mesh sensitivity test of the model*

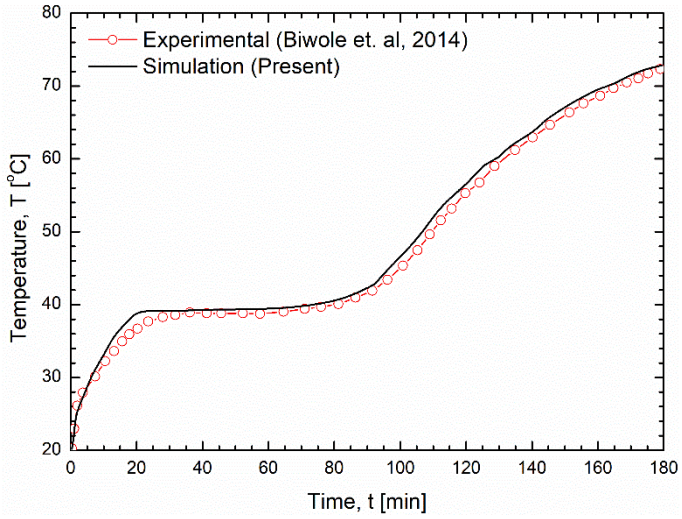


*Figure 5 Validation of numerical model with experimental study of Biwole et al* [31]

## 4. RESULTS AND DISCUSSION

The findings of this study are described in four different subsections. In the first one, the temperature variation in each cell and the whole computational domain, as well as the

observed evolution of the melt fraction are discussed, for a single honeycomb cell size and container's angle of inclination. In the next subsections, the effect of honeycomb cell size, container tilt angle, and honeycomb fin thickness are discussed. In the present study three factors are used to evaluate the efficiency of charging and discharging of PCM: (*i*) the average temperature of the front surface, which must keep on the lowest possible value for the longest possible time, (*ii*) the melt fraction of the PCM with time, (*iii*) the time-dependent energy storage content with a 1,000 W/m$^2$ constant heat flux on the front surface of the computational domain.

The melt fraction of the PCM in the computational domain is defined as:

$$\phi = \frac{Volume\ of\ the\ melted\ PCM\ \left(T>(T_m+\Delta T/2)\right)}{Total\ volume\ of\ PCM} \tag{11}$$

The energy stored in the PCM is calculated based on the temperature of the PCM.

$$\text{for}\quad T < T_m: E = mC_p(T - T_{ini}) \tag{12}$$

$$\text{for}\quad T = T_m: E = m\{C_p(T_m - T_{ini}) + L_f\} \tag{13}$$

$$\text{for}\quad T > T_m: E = m\{C_p(T_m - T_{ini}) + L_f + C_p(T - T_m)\} \tag{14}$$

Hear $E$ is energy storage content and $m$ is the mass of the PCM filled in the computational domain. The amount of energy stored in the melted PCM is computed as the energy stowed in entire numerical elements plus the computational domain.

## *4.1. Melting of PCM in honeycomb cells*

The PCM's melting in honeycomb cells is presented in Figure 6, at different time intervals with 0.015 m cell length and 0.0005 m honeycomb fin thickness. The color contours represent the variation of temperature, arrows show the velocity field, and the white line denotes the melting front of the PCM. The heat flux applied to the front (left) surface of the computational domain heats the PCM filled in the cells near the front surface. The PCM starts melting and melted PCM moves upward due to the buoyancy force and collects at the top of each cell. It can also be noted that the thermal behavior on each cell is related to that of its vertical neighbors. Despite the fact that they receive the same normal heat flux from the left,

316 the cells situated at the top of the container heat up faster than the cells situated at the bottom.
317 The warmer liquid PCM collected at the top of each cell, thus warming the cell directly
318 above, also explains this. For all these reasons, a double temperature gradient is observed
319 from top to bottom both in each cell and in the PCM container. As expected, a horizontal
320 temperature gradient in the container is also noted as the heat propagates from the heated
321 plate.

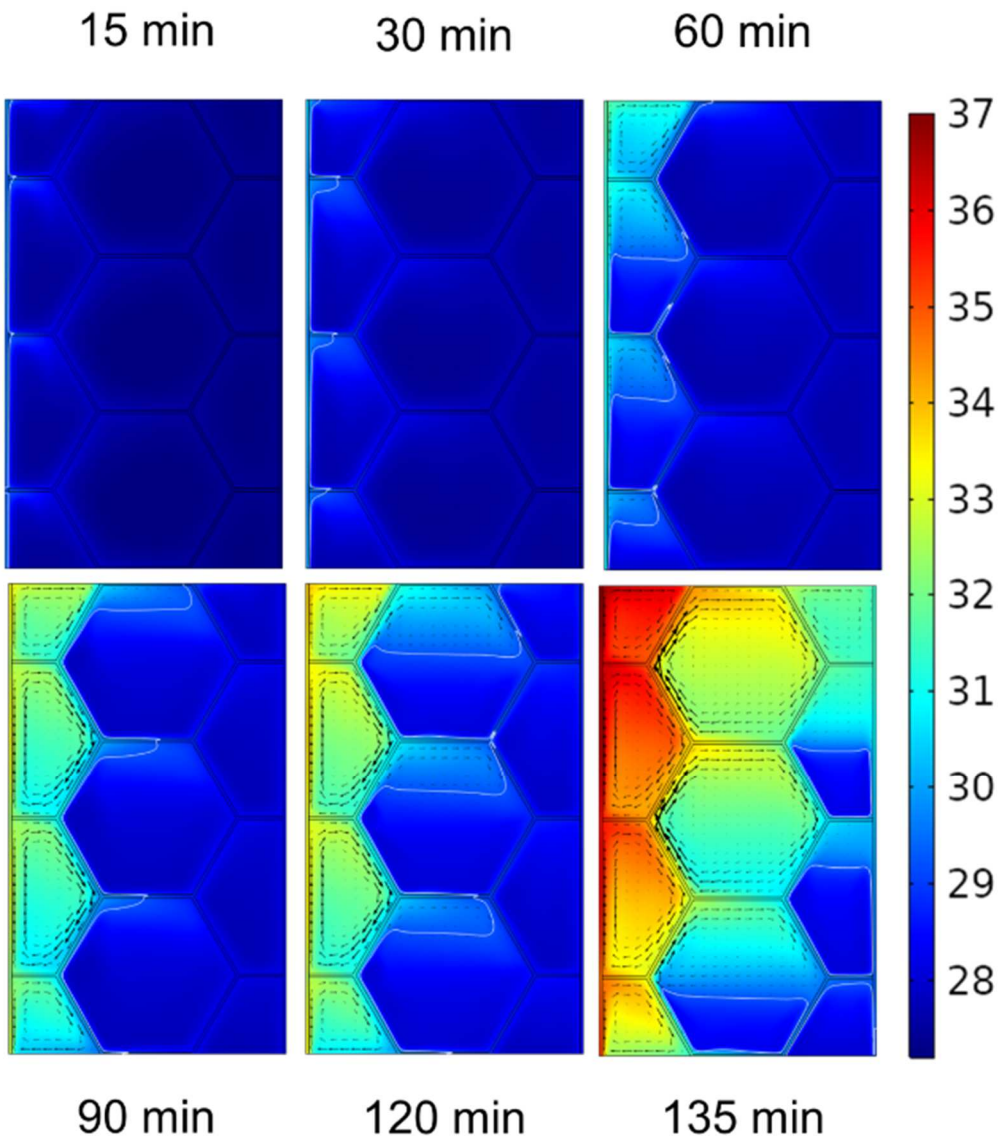


322

323 *Figure 6 Temperature field, melting front (white contours) and moving direction (black*
324 *arrows) of n-octadecane in honeycomb cells at different times*

325 The average temperature variation of the front and back surfaces, as well as the variation of
326 melt fraction ($\phi$) with time, are presented in Figure 7. The two inflexion points noted on the

curves of each surface average temperature are explained by the start and end of the PCM melting in the container, as obvious when comparing with the melt fraction curve. At first, the average front surface temperature increases sharply up to the melting temperature of the PCM. Then, it increases more gradually until the melt fraction of the PCM reaches its maximum value (i.e. 1). It resumes increasing sharply again as the heat storage is done in the form of sensible heat.

From $t$ = 60 min to $t$ = 90 min, a sudden increase in the front surface temperature of the computational domain is observed because of the complete melting of the cell near the front surface, which affects the melting of the PCM in the other cells of the container. At the same time, it was observed that there is a gradual increment in the melt fraction of the PCM compared to the initial stage of melting. The average back surface temperature gradually increases from the start of melting until the complete melting of PCM. Except at the start and end of PCM melting, there is no sudden increment or decrement in its temperature variation.

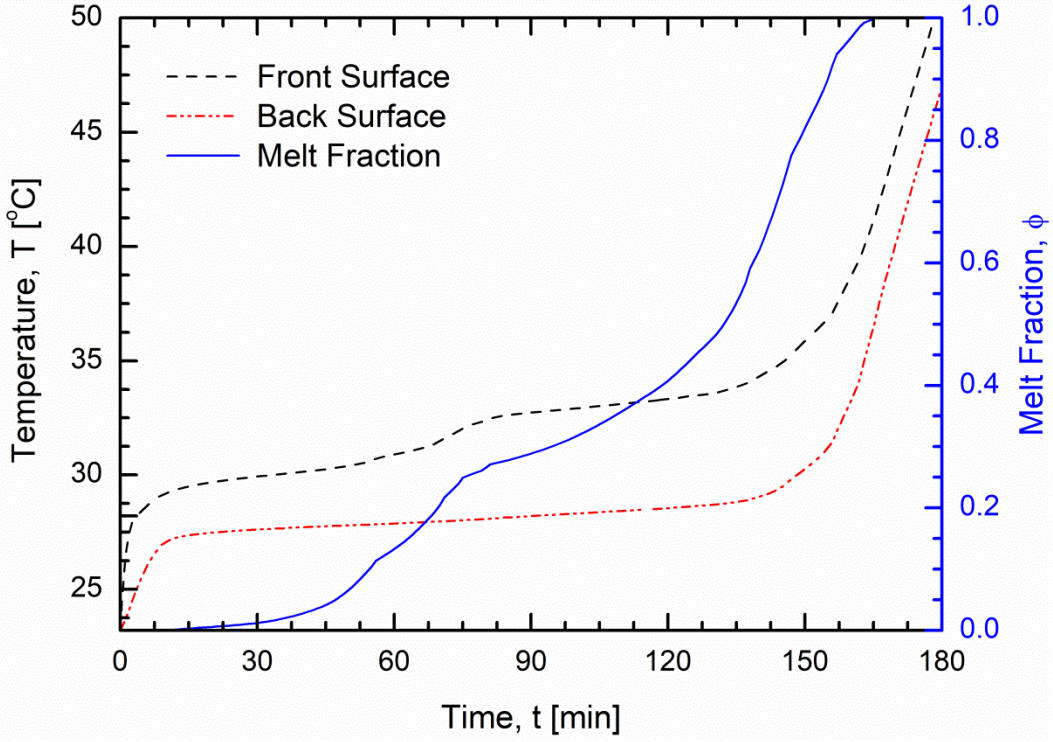


*Figure 7 Variation of melt fraction ($\phi$) and average front and back surface temperature of the container*

## *4.2. Effect of honeycomb cell size*

Figure 8 represents the temperature field, the melting front and shows the moving direction of the molten PCM in the computational domain for four different honeycomb cell sizes, at $t$ = 150 min for $\delta_{fin}$ = 0.0005 m and $\theta$ = 60°. For the smallest honeycomb cell size ($L_c$= 0.005 m), the PCM is completely melted, whereas for $L_c$ = 0.0075 m, 0.01 m and 0.015 m, some un-melted PCM remains. For the smaller cell sizes, the temperature gradient in the computational domain is reduced as compared to the larger cell sizes.

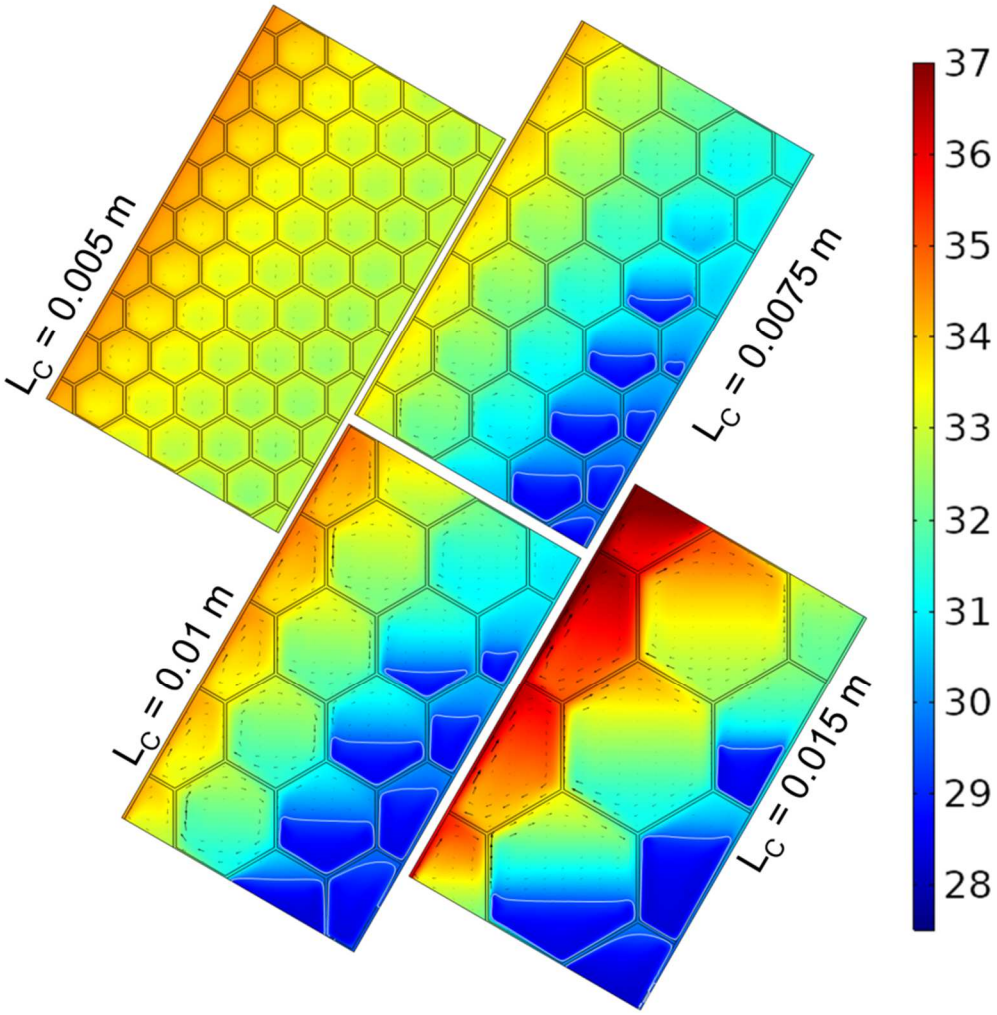


*Figure 8 Temperature field, melting front (white contours) and moving direction (black arrows) of n-octadecane in honeycomb container for different cell size at 150 min ($\delta_{fin}$ = 0.0005 m and $\theta$ = 60°)*

354 *4.2.1. Effect of honeycomb cell size on the average front surface temperature*

355 The average temperature variation of the front surface with time for different cell sizes and
356 angles of container inclination is presented in *Figure 9*. The comparison includes a case
357 without hexagonal cells in the computational domain. When the computational domain is
358 horizontal (*Figure 9*(a), $\theta = 0^o$), the average temperature of the front surface without
359 hexagonal cells increases sharply and reaches around 135 $^o$C at 180 min because of pure
360 conduction in the PCM. The effect of PCM is hardly noticeable. However with the
361 honeycomb heat exchanger at $L_c$ = 0.005 $m$, 0.0075 $m$, 0.01 $m$ and 0.015 $m$ the average front
362 surface temperature increases sharply only up to 30 $^oC$ at $t$ = 5 min, and then increases much
363 more gradually with time until $t$ = 150 min. This behavior is due to the presence of
364 hexagonal cells in the container that facilitates a smooth heat transfer in the PCM. The fin
365 structure transports heat all over the computational domain efficiently, thanks to its higher
366 thermal conductivity. An increment in the tilt angle results in an enhancement of the
367 convective heat transport in the PCM, which in turn further reduces the average front surface
368 temperature. It is also observed that the angle of inclinations have a minor effect when the
369 cell size is small ($L_C$ = 0.005 m, $L_C$ = 0.01 m and $L_C$ = 0.015 m). From *Figure 9*(a)-(d) it is
370 noted that the inclination angle only affects the average front surface temperature when the
371 cell size is large. A major influence of the inclination angle on average front surface
372 temperature is only observed when there are no hexagonal cells in the computational domain.
373 Due to the addition of honeycomb cells, it is possible to keep the front surface temperatures
374 at 32 $^o$C, which is around 90$^o$C below as compared to the horizontal case (i.e. $\theta = 0^o$, pure
375 conduction), 50$^o$C lower as compared to $\theta = 30^o$ case, 15$^o$C lower as compared to $\theta = 60^o$
376 case and 8$^o$C lower as compared to $\theta = 90^o$ case. It is also probable to keep an approximately
377 constant temperature of the front surface for up to 140 min.

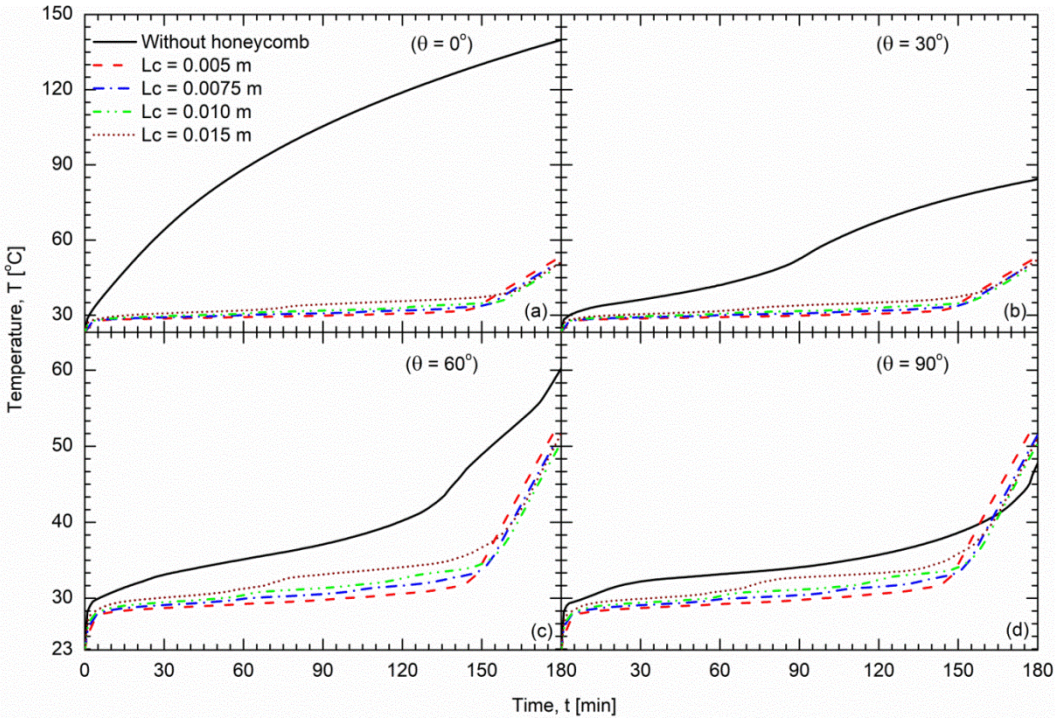


*Figure 9 Average front surface temperature variation with time for different honeycomb cell sizes: (a) at θ = 0°, (b) θ = 30° (c) θ = 60° and (d) θ = 90°*

### *4.2.2. Effect of honeycomb cell size on the melt fraction*

The variation of melt fraction in the computational domain for different cell sizes and various inclination angles is shown in Figure 10. Four disparate inclination angles (i.e. 0°, 30°, 60°, and 90°) are considered in the present study. The melt fraction without honeycomb cells is advanced as compared to that with honeycomb cells up to 140 min, regardless of the cell sizes. This behavior is observed because of two reasons. Firstly, the presence of honeycomb cells transfers heat to the entire computational domain, not only to the PCM available near the front heating surface. Due to the absorption of heat as sensible heat by the computational domain, the melt fraction of the PCM without cells is higher for a certain time and melting starts later for the smallest cell size as compared to larger cell size. Secondly, in the beginning, the convection heat transfer is accentuated in the configuration without cells, since the melt PCM has more room for movement. After a certain amount of time (140 min here), the latter convection process fails to achieve fast melting of the solid PCM situated as the bottom left of the container and becomes less efficient than that of celled configurations where heat is transported everywhere, as shown in Figure 8.

The latter reasoning holds when comparing meshed configurations. One can observe that for cases with higher cell sizes, melting starts earlier but ends later than for smaller cell sizes. As the heat which is transferred from the heated surface to the entire computational domain is reduced with larger cells, their initially higher melting rate decreases, and they finally take a longer time to achieve complete melting. For all the inclination angles it is observed that the melting starts at around 60 min, 35 min, 20 min, and 10 min for $L_c$ = 0.005 m, $L_c$ = 0.0075 m, $L_c$ = 0.01 m, and $L_c$ = 0.015 m respectively, meaning that the finer the mesh, the later the melting start.

There are several inflection points observed in the melt fraction variation for all the cell sizes and inclination angles. The first inflection point for $L_c$ = 0.005 m, $L_c$ = 0.0075 m, $L_c$ = 0.01 m, and $L_c$ = 0.015 m is observed when melt fraction reaches around 0.1, 0.15, 0.2 and 0.3 respectively. The second inflection point in the melt fraction is not observed when $L_c$ = 0.015, however for $L_c$ = 0.005 m, $L_c$ = 0.0075 m, $L_c$ = 0.01 m the inflection point is observed when the melt fraction reaches 0.225, 0.45, and 0.55 respectively. The number of inflection points in the melt fraction variation depends on the number of cells in the direction of the heat flux application. The inflections in the melt fraction are because of the uneven heat transfer that happened simultaneously by the additional contact resistance at the surface of each cell and to convection in the melted PCM within the cells. Regarding the latter cause, the heat transfer to the honeycomb cell is faster when the PCM filled in the previous cell is completely melted. If the PCM filled in the previous cell is not completely melted, the heat is absorbed by the solid PCM and a reduced amount of energy is transferred to the next cell which reduces the melting rate in that cell, resulting in a reduced melt fraction.

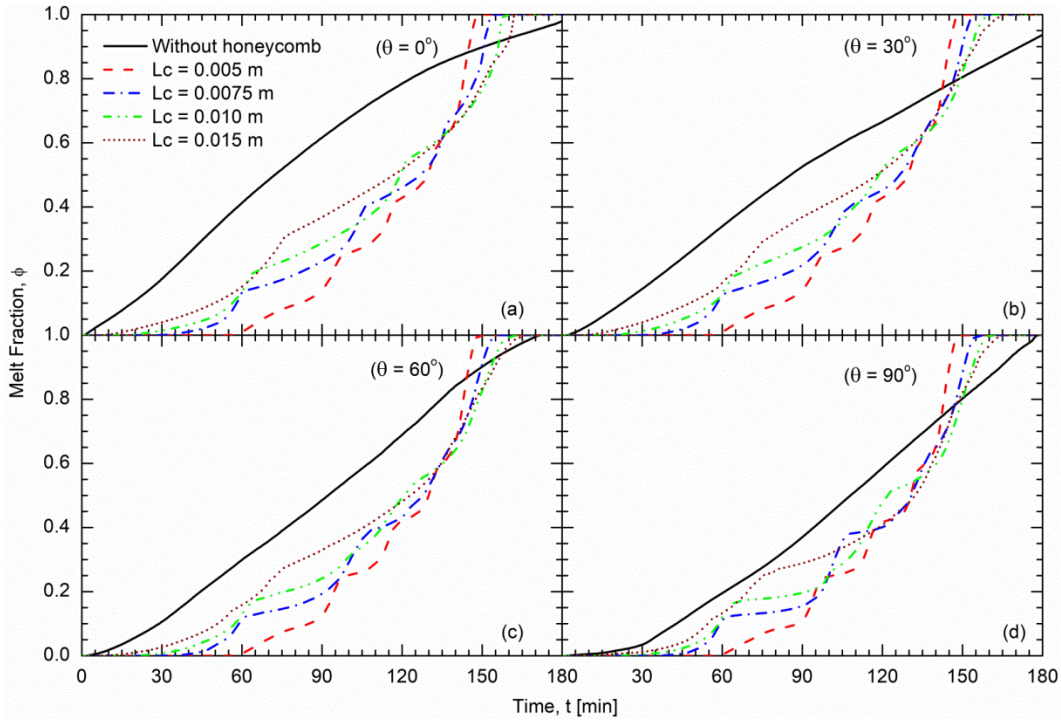


*Figure 10 Melt fraction variation with time for different honeycomb cell sizes: (a) at $\theta = 0^o$, (b) $\theta = 30^o$ (c) $\theta = 60^o$ and (d) $\theta = 90^o$*

### *4.2.3. Effect of honeycomb cell size on the energy stored*

The energy stored is calculated for different cell sizes and tilt angles, as presented in Figs. Figure 11(a)-(d). The maximum energy is stored for the computational domains that have no hexagonal cells because, without honeycomb cells, the temperature of the computational domain is higher as compared to other configurations, which results in additional energy stored in as sensible heat. The honeycomb cells facilitate the heat transfer to the backplate and the environment beyond, thus reducing the thermal energy remaining in the container. The decrease in the cell size causes an increased number of cells in the computational domain, which reduces the actual volume of the PCM in the container. Therefore, finer mesh configurations exhibit a lower heat storage capacity. For meshed configurations, it is also observed that the inclination angle does not significantly affect the energy content in the PCM.

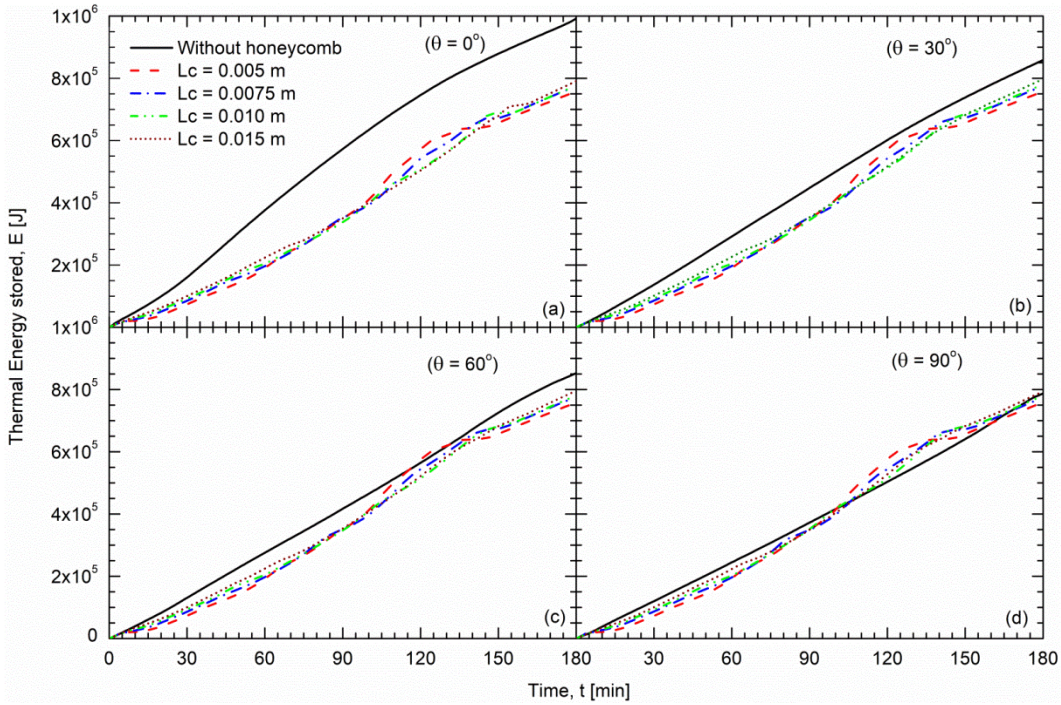


*Figure 11 Energy stored in PCM with time for different honeycomb cell sizes: (a) at θ = 0o, (b) θ = 30o (c) θ = 60o and (d) θ = 90o*

## *4.3. Effect of the inclination angle*

The melting of PCM in a rectangular container also depends on the inclination angle due to the convection effect. The effect of the tilt angle of the computational domain from horizontal on the average temperature of the front surface, melt fraction, energy stored in the container is presented for two different cell sizes, $L_C = 0.015\ m$ and $L_C = 0.0075\ m$.

### *4.3.1. Influence of inclination angle on the average front surface temperature*

Figure 12(a) and (d) show the average front surface temperature variation at different angles of inclination for two different cell sizes $L_C = 0.015\ m$ and $L_C = 0.0075\ m$, respectively. For both cell sizes, the minimum average front surface temperature is obtained with $\theta = 90^o$ because of higher convective heat transfer in the computational domain. The impact of the angle of inclination on the average front surface temperature is negligible with smaller cell sizes because of the enhanced thermal transport due to the existence of the fin structure. The presence of the fin structure reduces the velocity field; however, it enhances thermal transport via the metallic structure.

450 *4.3.2. Influence of inclination angle on the melt fraction*

451 The Influence of the tilt angle of the computational domain on the melt fraction for two
452 different cell sizes is presented in Figures 12(b) and (e). For a certain time duration, the melt
453 fraction is advanced when the computational domain is completely horizontal ($\theta$ = 0$^{o}$) for
454 both cell sizes. Further, there are inflection points in the melting curve of both cell sizes. As
455 previously mentioned, this is due to the uneven heat transfer that happened because of the
456 additional contact resistance at the surface of each cell and to convection in the melted PCM
457 within the cells. The number of inflection points in the melt fraction depends on the number
458 of hexagonal cells present in the computational domain.

459 *4.3.3. Influence of inclination angle on the energy stored*

460 The energy storage content in the PCM with time at different inclination angles is presented
461 in Figure 12(c) and (f) for $L_C$ = 0.015 m and $L_C$ = 0.0075 m, respectively. There is a small
462 variation are observed for the different angle of inclination during energy storage with $L_C$ =
463 0.015 m, however, there is no variation with $L_C$ = 0.0075 m. for given cell size and fin
464 thickness the overall rate of energy storage is the same, regardless of the angle of inclination.
465 This is due to the hypothesis of normal heat flux on the front surface in all configurations.
466 The results might be different in real applications where the amount of solar radiation
467 received depends on the container's tilt angle.

468

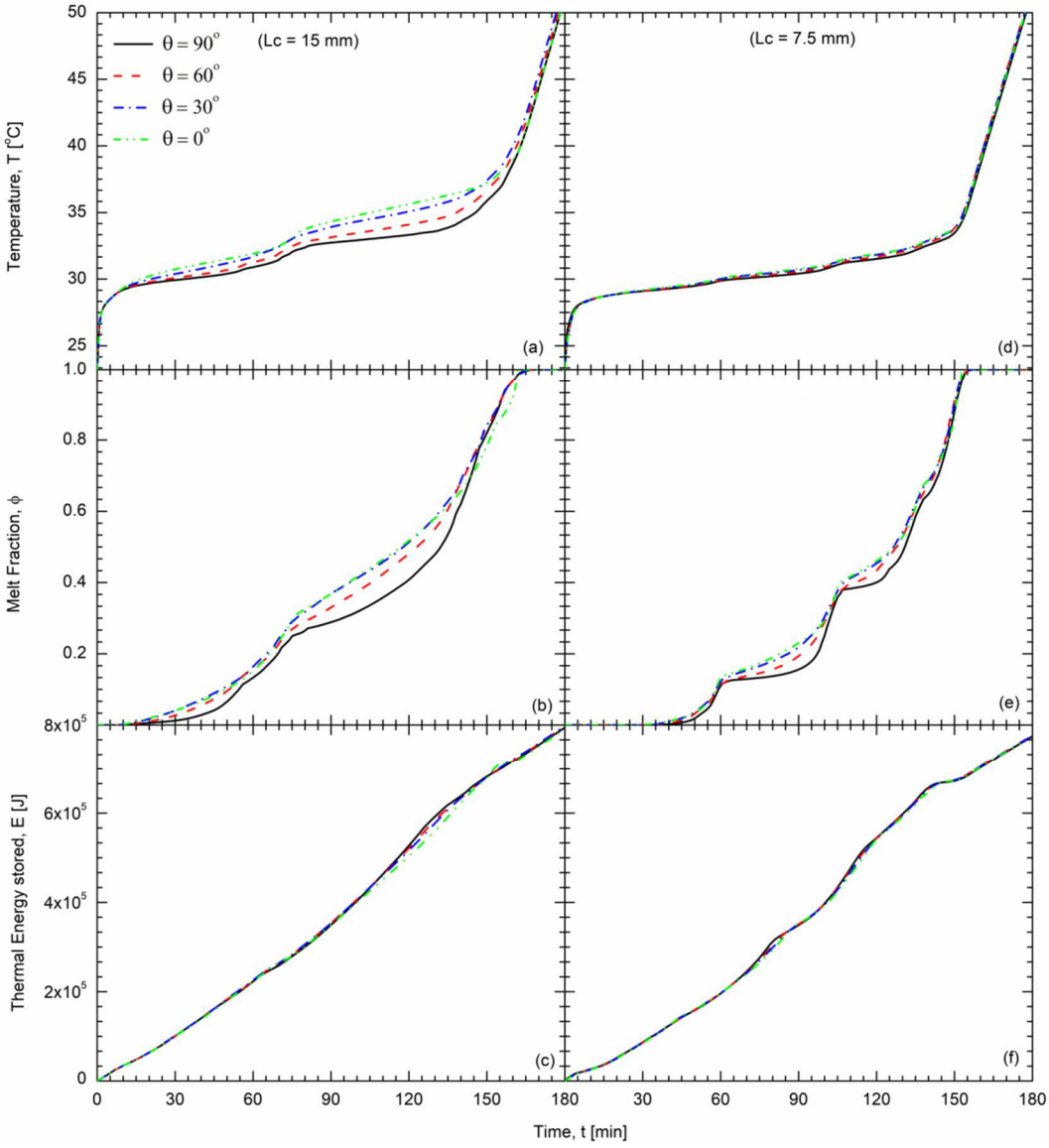


*Figure 12 Effect of tilt angle on average front surface temperature, melt faction and energy stored in the PCM: (a)-(c) $L_C$ = 0.015 m, (d)-(f) $L_C$ = 0.0075 m*

## *4.4. Effect of the honeycomb cell fin thickness*

### *4.4.1. Effect of the honeycomb cell fin thickness on the average front surface temperature*

*Figure 13* represents the average front surface temperature variation for four different honeycomb cell fin thicknesses (i.e. $\delta_{fin} = 0.25\ mm, 0.5\ mm, 1\ mm\ and\ 1.5\ mm$). Four different cell sizes are also considered. *Figure 13* (a) represents the average temperature variation for $L_C$ = 0.005 m. At first, the minimum temperature is obtained with a thicker fin because of higher heat transmission to the backplate. But due to enhanced heat transfer to the PCM and reduced volume of PCM in the container, the thicker fin configuration is also the

one with a shorter melting time and its average front surface temperature becomes highest after the complete melting of PCM. The same behavior is observed for all fin thicknesses, with the inversion depending on the fin thickness, except before the end of melting where there is a very small temperature difference for $\delta_{fin} = 0.5\,mm, 1\,mm\ and\ 1.5\,mm$. As shown in *Figure 13* (b)-(d) the cell size does not significantly change the above-described pattern. However larger cell sizes reduce thermal transport to the PCM and therefore, the average front surface temperature is higher for the higher cell size.

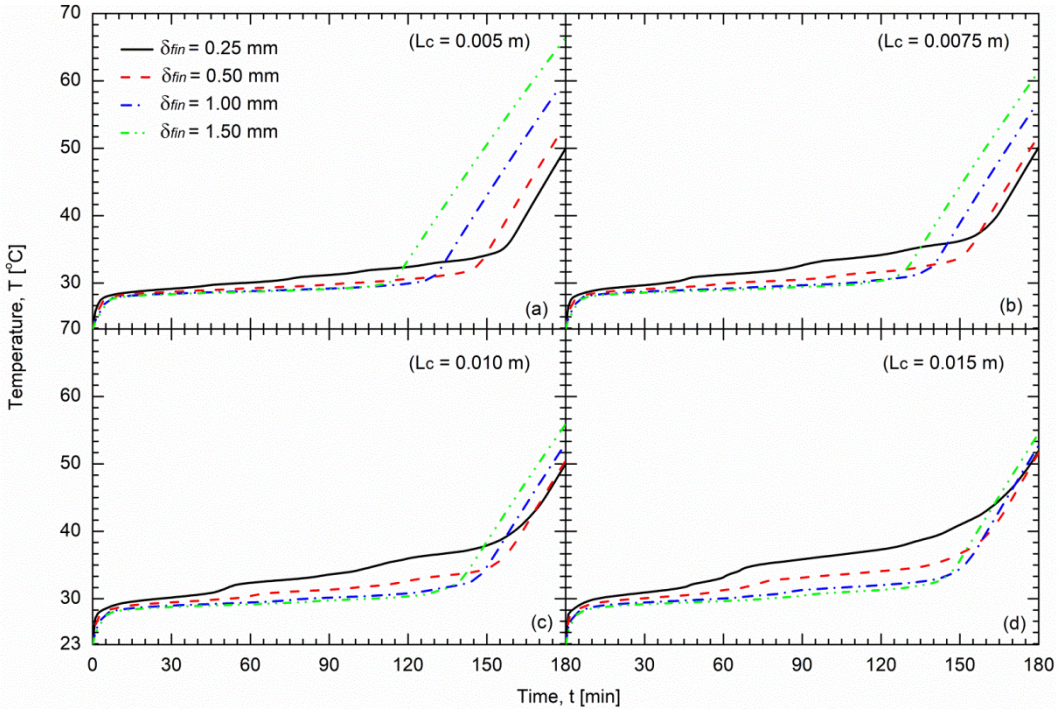


*Figure 13 Average front surface temperature variation with time at different honeycomb fin thickness: (a) at $L_C$ = 0.005 m, (b) $L_C$ = 0.0075 m (c) $L_C$ = 0.010 m and (d) $L_C$ = 0.015 m*

*4.4.2. Effect of the honeycomb cell fin thickness on the melt fraction*

The effect of honeycomb cell fin thickness on melt fraction for different cell sizes is shown in Figure 14(a)-(d). Figure 14(a) represents the melt fraction at $L_C$ = 0.005 m for different fin thicknesses. The melting of PCM starts later for higher fin thicknesses as compared to lower ones, because of the higher fin thickness transport to the backplate and higher storage of sensible heat in the fins. Due to sensible heating below the melting temperature, the melting of PCM starts later which can be visible in Figure 14(a). Similar to the previous subsection, after fin sensible heating, the heat transfer is enhanced with higher fin thickness, with less volume of PCM, which explains the end of melting, earlier than that of lower fin thicknesses.

A similar pattern is obtained with all other cell sizes; however, the complete melting time is higher for higher cell sizes.

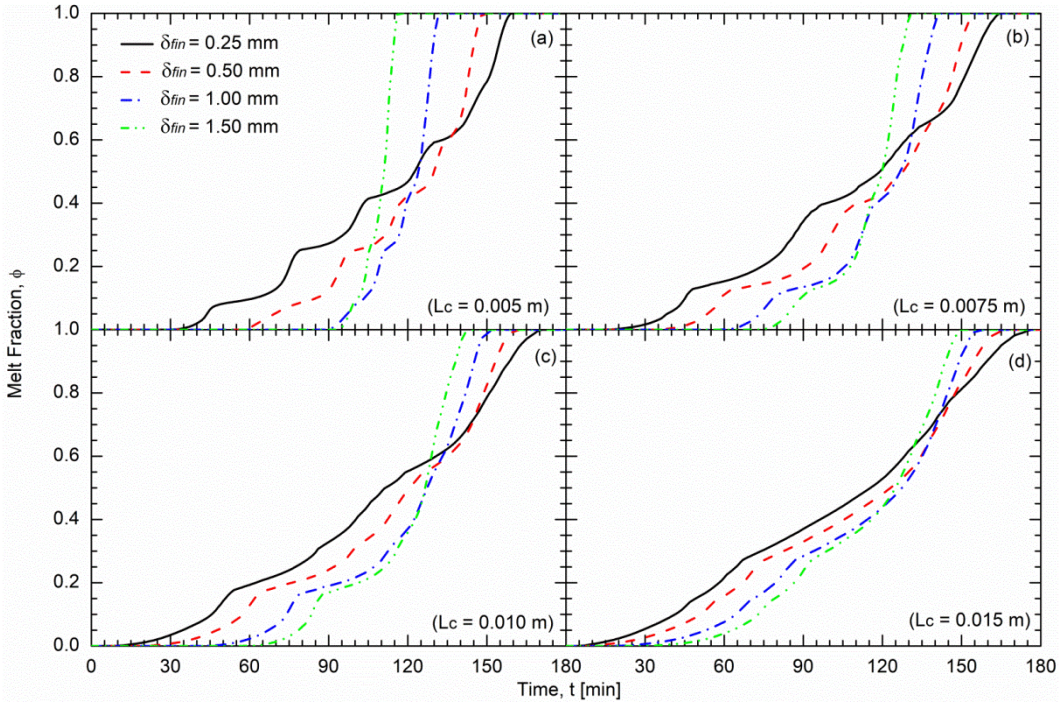


*Figure 14 Melt fraction variation with time at different honeycomb fin thickness: (a) at $L_C$ = 0.005 m, (b) $L_C$ = 0.0075 m (c) $L_C$ = 0.010 m and (d) $L_C$ = 0.015 m*

*4.4.2. Effect of the honeycomb cell fin thickness on the energy stored*

The variation of energy storage content in the computational domain with time for different fin thicknesses for four different cell sizes is presented in Figure 15(a)-(d). Initially, the energy storage rate in the PCM is higher for smaller fin thicknesses, as the energy is quickly transported to the PCM (reduced sensible heat accumulation in the fins). After the melting of PCM starts, it becomes lower for lower fin thicknesses, as previously explained. The overall energy storage content after complete melting is higher for lower fin thickness and minimum for highest fin thickness because of the reduction in the actual volume of PCM filled in the computational domain. Increasing the cell size tends to reduce the effect of fin thickness, as the rate of energy storage becomes similar for all cases (Figure 15 (c)-(d)).

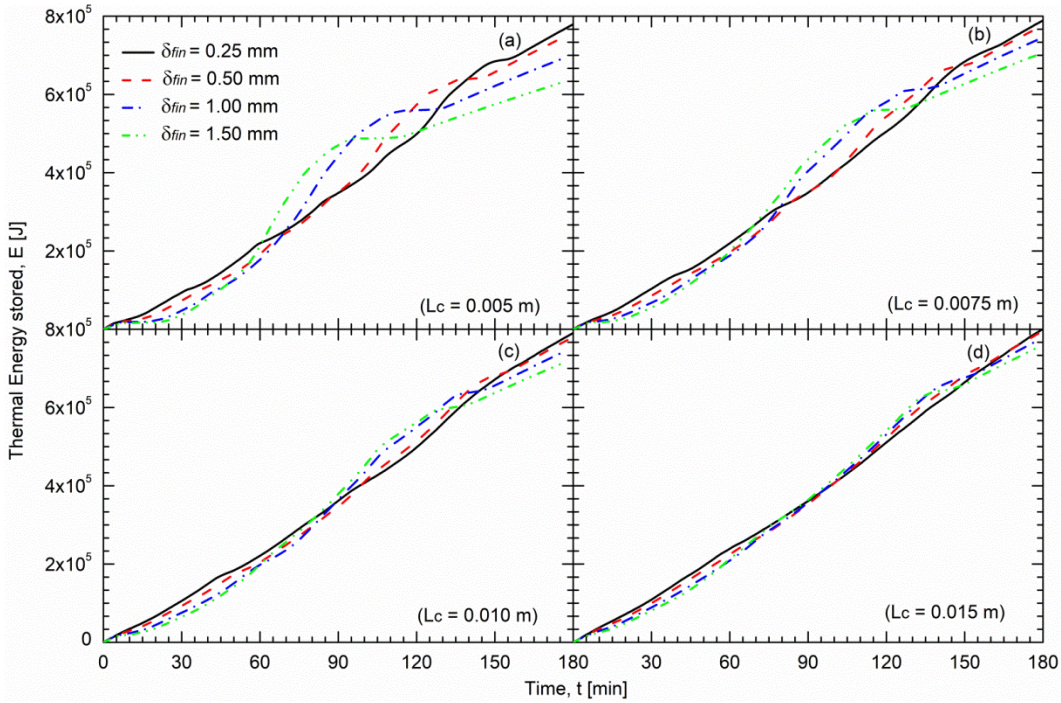


*Figure 15 Energy stored in PCM with time at different honeycomb fin thickness: (a) at $L_C$ = 0.005 m, (b) $L_C$ = 0.0075 m (c) $L_C$ = 0.010 m and (d) $L_C$ = 0.015 m*

## 5. Conclusions

In the current study, the influence of honeycomb meshed fins on the heat transport performance of a rectangular PCM container inclined at different angles from horizontal has been numerically studied. A 2D numerical model of the rectangular container with honeycomb structure considering conduction and convection modes of heat transfer in the melted PCM is developed. The heat transfer and energy storage behavior without honeycomb cells was looked up to that of four other configurations where the PCM is filled in honeycomb cells of four different lengths, thicknesses, and tilted at four different inclination angles. The evaluation of the charging and discharging efficiency of the PCM-filled in honeycomb fins structures were based on the melting time, the regulation of the front plate temperature to retain it as low as possible for the longest possible duration, as well as the energy storage rate.

Results have shown that natural convection plays an important role in maintaining the average temperature of the front surface to a constant value and for continuous thermal transport in PCM. Further, optimized honeycomb cell length and fin thickness choices would be vital for a rapid heat transfer to the rear end of the computational domain. It was also

found that a tilt angle of the honeycomb cells has a minor influence on the heat transfer behavior of all studied patterns when the cell size is small. The total melting time is minimum for lower cell sizes and higher fin thickness regardless of the orientation of the computational domain. With such a configuration, it is possible to keep the front surface temperatures at 32 $^{o}$C, which is around 90$^{o}$C lower compared to the horizontal case (pure conduction, $\theta = 0^{o}$). The energy storage behavior of the PCM with varying time is also investigated for the range of parameters selected in the present study and it is found that the total energy content is higher without honeycomb mesh because of the higher amount of PCM, while the tilt angle has a marginal effect on the energy storage rate in cases where the heat flux remains normal to the heated surface. Finally, it is concluded that this type of fin structure leads to enhanced thermal transport in the PCM to maintain the front surface temperature constant. Besides, the charging and discharging time of PCM is reduced as compared to without meshed configuration. Overall, such studies for PCM encapsulated in honeycomb cells may be utilized for appropriate thermal management and to optimize heat transfer and energy storage.

## Declaration of competing interest

The authors have no conflict of interest regarding this work.

## Acknowledgment

The authors want to acknowledge the Université Clermont Auvergne postdoctoral grant 2020-2021.

555 # References


556 [1] X. Qiao, X. Kong, H. Li, L. Wang, H. Long, Performance and optimization of a novel
557 active solar heating wall coupled with phase change material, Journal of Cleaner
558 Production. (2020). https://doi.org/10.1016/j.jclepro.2019.119470.

559 [2] X. Kong, L. Wang, H. Li, G. Yuan, C. Yao, Experimental study on a novel hybrid
560 system of active composite PCM wall and solar thermal system for clean heating
561 supply in winter, Solar Energy. (2020). https://doi.org/10.1016/j.solener.2019.11.081.

562 [3] S. Gorjian, F. Calise, K. Kant, M.S. Ahamed, B. Copertaro, G. Najafi, X. Zhang, M.
563 Aghaei, R.R. Shamshiri, A review on opportunities for implementation of solar energy
564 technologies in agricultural greenhouses, Journal of Cleaner Production. 285 (2021)
565 124807. https://doi.org/10.1016/j.jclepro.2020.124807.

566 [4] K. Kant, A. Shukla, A. Sharma, A. Kumar, A. Jain, Thermal energy storage based
567 solar drying systems: A review, Innovative Food Science & Emerging Technologies.
568 34 (2016) 86–99. https://doi.org/10.1016/j.ifset.2016.01.007.

569 [5] A. Shukla, A. Sharma, K. Kant, Solar greenhouse with thermal energy storage: A
570 review, Current Sustainable/Renewable Energy Reports. 3 (2016) 58–66.
571 https://doi.org/10.1007/s40518-016-0056-y.

572 [6] Y. Dutil, D.R. Rousse, N. Ben Salah, S. Lassue, L. Zalewski, A review on phase-
573 change materials: Mathematical modeling and simulations, Renewable and Sustainable
574 Energy Reviews. 15 (2011) 112–130. https://doi.org/10.1016/j.rser.2010.06.011.

575 [7] K. Kant, A. Shukla, A. Sharma, P. Henry Biwole, Heat transfer study of phase change
576 materials with graphene nano particle for thermal energy storage, Solar Energy. 146
577 (2017) 453–463. https://doi.org/10.1016/j.solener.2017.03.013.

578 [8] K. Kant, A. Anand, A. Shukla, A. Sharma, Heat transfer study of building integrated
579 photovoltaic (BIPV) with nano-enhanced phase change materials, Journal of Energy
580 Storage. 30 (2020) 101563. https://doi.org/10.1016/j.est.2020.101563.

581 [9] X. Tong, J.A. Khan, M. Ruhul Amin, Enhancement of heat transfer by inserting a
582 metal matrix into a phase change material, Numerical Heat Transfer, Part A:
583 Applications. 30 (1996) 125–141. https://doi.org/10.1080/10407789608913832.

584 [10] J.M. Marín, B. Zalba, L.F. Cabeza, H. Mehling, Improvement of a thermal energy
585 storage using plates with paraffin-graphite composite, International Journal of Heat

586 and Mass Transfer. (2005). https://doi.org/10.1016/j.ijheatmasstransfer.2004.11.027.

587 [11] H.A. Adine, H. El Qarnia, Numerical analysis of the thermal behaviour of a shell-and-
588 tube heat storage unit using phase change materials, Applied Mathematical Modelling.
589 33 (2009) 2132–2144. https://doi.org/10.1016/j.apm.2008.05.016.

590 [12] Y. Tian, C.Y. Zhao, Thermal and exergetic analysis of Metal Foam-enhanced
591 Cascaded Thermal Energy Storage (MF-CTES), International Journal of Heat and
592 Mass Transfer. (2013). https://doi.org/10.1016/j.ijheatmasstransfer.2012.11.034.

593 [13] P.H. Biwole, D. Groulx, F. Souayfane, T. Chiu, Influence of fin size and distribution
594 on solid-liquid phase change in a rectangular enclosure, International Journal of
595 Thermal Sciences. (2018). https://doi.org/10.1016/j.ijthermalsci.2017.10.038.

596 [14] D. Groulx, P.H. Biwole, M. Bhouri, Phase change heat transfer in a rectangular
597 enclosure as a function of inclination and fin placement, International Journal of
598 Thermal Sciences. (2020). https://doi.org/10.1016/j.ijthermalsci.2020.106260.

599 [15] A.A. Rabienataj Darzi, M. Jourabian, M. Farhadi, Melting and solidification of PCM
600 enhanced by radial conductive fins and nanoparticles in cylindrical annulus, Energy
601 Conversion and Management. 118 (2016) 253–263.
602 https://doi.org/10.1016/j.enconman.2016.04.016.

603 [16] S. Mat, A.A. Al-Abidi, K. Sopian, M.Y. Sulaiman, A.T. Mohammad, Enhance heat
604 transfer for PCM melting in triplex tube with internal-external fins, Energy Conversion
605 and Management. (2013). https://doi.org/10.1016/j.enconman.2013.05.003.

606 [17] M. Sheikholeslami, S. Lohrasbi, D.D. Ganji, Numerical analysis of discharging
607 process acceleration in LHTESS by immersing innovative fin configuration using
608 finite element method, Applied Thermal Engineering. (2016).
609 https://doi.org/10.1016/j.applthermaleng.2016.06.158.

610 [18] L. Wu, X. Zhang, X. Liu, Numerical analysis and improvement of the thermal
611 performance in a latent heat thermal energy storage device with spiderweb-like fins,
612 Journal of Energy Storage. 32 (2020) 101768.
613 https://doi.org/10.1016/j.est.2020.101768.

614 [19] Y. Chen, Z. Deng, Hydrodynamics of a droplet passing through a microfluidic T-
615 junction, Journal of Fluid Mechanics. (2017). https://doi.org/10.1017/jfm.2017.181.

616 [20] C. Zhang, F. Yu, X. Li, Y. Chen, Gravity–capillary evaporation regimes in

617 microgrooves, AIChE Journal. (2019). https://doi.org/10.1002/aic.16484.

618 [21] M. Liu, L. Su, J. Li, S. Chen, Y. Liu, J. Li, B. Li, Y. Chen, Z. Zhang, Investigation of
619 spherical and concentric mechanism of compound droplets, Matter and Radiation at
620 Extremes. (2016). https://doi.org/10.1016/j.mre.2016.07.002.

621 [22] Y. Chen, C. Zhang, M. Shi, Y. Yang, Thermal and hydrodynamic characteristics of
622 constructal tree-shaped minichannel heat sink, AIChE Journal. (2010).
623 https://doi.org/10.1002/aic.12135.

624 [23] C. Zhang, Y. Chen, R. Wu, M. Shi, Flow boiling in constructal tree-shaped
625 minichannel network, International Journal of Heat and Mass Transfer. (2011).
626 https://doi.org/10.1016/j.ijheatmasstransfer.2010.09.051.

627 [24] X. Daguenet-Frick, J. Bonjour, R. Revellin, Constructal microchannel network for
628 flow boiling in a disc-shaped body, IEEE Transactions on Components and Packaging
629 Technologies. (2010). https://doi.org/10.1109/TCAPT.2009.2027427.

630 [25] R. Wu, Y.P. Chen, J.F. Wu, M.H. Shi, Flow boiling characteristics in constructal tree-
631 shaped minichannel, Kung Cheng Je Wu Li Hsueh Pao/Journal of Engineering
632 Thermophysics. (2010).

633 [26] A. Sciacovelli, F. Gagliardi, V. Verda, Maximization of performance of a PCM latent
634 heat storage system with innovative fins, Applied Energy. (2015).
635 https://doi.org/10.1016/j.apenergy.2014.07.015.

636 [27] C. Zhang, J. Li, Y. Chen, Improving the energy discharging performance of a latent
637 heat storage (LHS) unit using fractal-tree-shaped fins, Applied Energy. (2020).
638 https://doi.org/10.1016/j.apenergy.2019.114102.

639 [28] J. LI, Y. Huang, C. Zhang, X. Liu, Numerical study on the solidification performance
640 of a latent heat storage unit with Koch-fractal fin, Fractals. 27 (2019) 1950108.
641 https://doi.org/10.1142/S0218348X19501081.

642 [29] M. Sheikholeslami, S. Lohrasbi, D.D. Ganji, Response surface method optimization of
643 innovative fin structure for expediting discharging process in latent heat thermal
644 energy storage system containing nano-enhanced phase change material, Journal of the
645 Taiwan Institute of Chemical Engineers. (2016).
646 https://doi.org/10.1016/j.jtice.2016.08.019.

647 [30] K. Kant, A. Shukla, A. Sharma, P.H. Biwole, Heat transfer studies of photovoltaic

panel coupled with phase change material, Solar Energy. 140 (2016) 151–161. https://doi.org/10.1016/j.solener.2016.11.006.

[31] P.H. Biwole, P. Eclache, F. Kuznik, Phase-change materials to improve solar panel's performance, Energy and Buildings. 62 (2013) 59–67. https://doi.org/10.1016/j.enbuild.2013.02.059.

[32] H. Shokouhmand, B. Kamkari, Experimental investigation on melting heat transfer characteristics of lauric acid in a rectangular thermal storage unit, Experimental Thermal and Fluid Science. (2013). https://doi.org/10.1016/j.expthermflusci.2013.06.010.

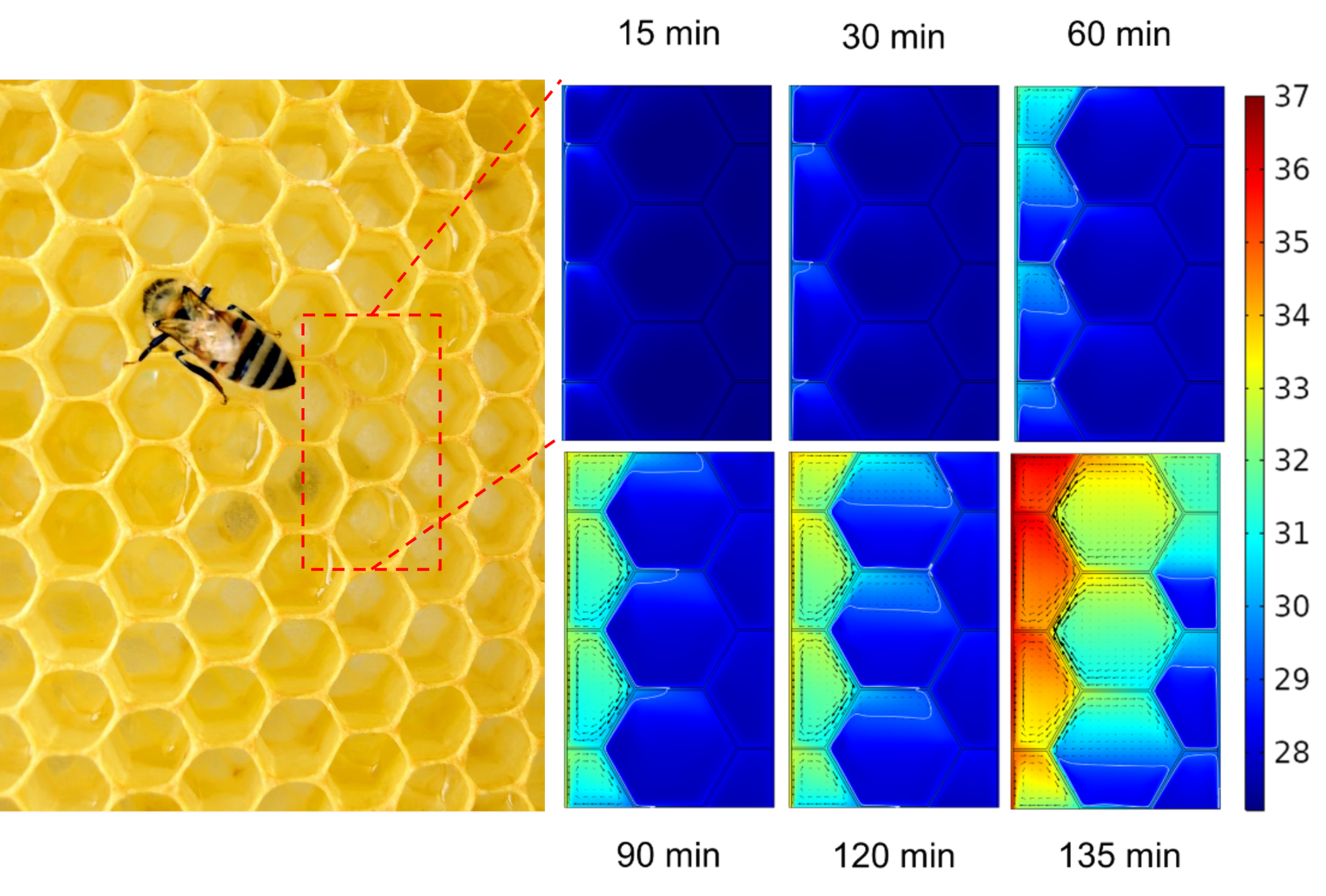
15 min
30 min
60 min
90 min
120 min
135 min
37
36
35
34
33
32
31
30
29
28